Mathematical Biosciences 271 (2016) 118–127

Contents lists available at ScienceDirect

Mathematical Biosciences

journal homepage: www.elsevier.com/locate/mbs

Three-dimensional simulations of the cell growth and cytokinesis using the immersed boundary method

Yibao Li [a], Junseok Kim [b,*]

[a] School of Mathematics and Statistics, Xi'an Jiaotong University, Xi'an 710049, China
[b] Department of Mathematics, Korea University, Seoul 136-701, Republic of Korea

ARTICLE INFO

Article history:
Received 10 March 2015
Revised 12 September 2015
Accepted 16 November 2015
Available online 1 December 2015

Keywords:
Cytokinesis
Cleavage furrow
Immersed boundary method
Volume correction algorithm
Surface remeshing algorithm

ABSTRACT

In this paper, we present a three-dimensional immersed boundary method to simulate the eukaryotic cell growth and cytokinesis. The proposed model and numerical method are a non-trivial three-dimensional extension of the previous work (Li et al., 2012). Unstructured triangular meshes are employed to discretize the cell membrane. The nodes of the surface mesh constitute a set of Lagrangian control points used to track the motion of the cell. A surface remeshing algorithm is applied to prevent mesh distortion during evolution. We also use a volume-conserving algorithm to maintain the mass of cells in cytokinesis. The ability of the proposed method to simulate cell growth and division processes is numerically demonstrated.

1. Introduction

Cell growth and division are fundamental phenomena that generate and maintain all life. The study of these phenomena is vital to understanding the basic processes of life by which an organism is built. In the eukaryotic cell cycle, mitosis is the phase that occurs between DNA replication and the formation of two daughter cells. There are four stages of mitosis: prophase, metaphase, anaphase, and telophase. The first and longest stage of mitosis is prophase. During prophase, two aster-covered centrosomes migrate to opposite sides of the nucleus in preparation of mitotic spindle formation. During metaphase, the kinetochore microtubules connect to the centromere. Next, during anaphase, the kinetochore microtubules pull the chromosomes apart into individual chromatids and pull them towards the centrosomes located at opposite ends of the cell. This allows the cell to divide properly to ensure that each daughter cell contains full replicas of chromosomes [2].

The final stage of cell division is cytokinesis. During cytokinesis, the cell divides into two daughter cells. In the case of animal cells, the membrane of the parent cell pinches inward along the cell's equator until the two daughter cells are formed, i.e., one animal cell separates into two by the contractile ring, which is formed by actin–myosin interactions. The contractile ring forms a cleavage furrow, and as the contractile ring tightens, the cleavage furrow develops further. Eventually, the cell divides into two daughter cells.

Until recently, many studies have focused on cell motion and cell cytokinesis [3–24]. Among these studies, determining the site of cell division is an active problem in cell biology. To numerically simulate cytokinesis, we consider the astral stimulation model [11,20], which states that signals from the astral centers have larger values at the overlapped equatorial positions. The division mechanism is formed by direct response in the stimulated region (see Fig. 1).

To study cell growth and cytokinesis, we propose a mathematical model for the growth and division of a single cell and simulate this governing model using an immersed boundary method in three-dimensional space, which is an extension of the work of Li et al. [24]. Li et al. proposed a realistic contractile force on the axisymmetric space. Note that the immersed boundary method, which is a mathematical formulation and numerical approach in computational biology, has been widely used [13–15,18,25,26].

Unlike the previous work [24], we implement the numerical algorithm on a fully three-dimensional space, which is a non-trivial extension of two-dimensional space. To discretize the cell membrane, we employ unstructured triangular meshes. The nodes of the surface mesh constitute a set of Lagrangian control points that are used to track the morphology of the cell. A surface remeshing algorithm [27] is applied to prevent mesh distortion during evolution. To maintain the mass of the cell in cytokinesis, we use a volume-conserving algorithm [28]. The ability of the method to simulate the cell growth and division processes is numerically demonstrated.

* Corresponding author. Tel.: +82 2 3290 3077; fax: +82 2 929 8562.
E-mail addresses: yibaoli@mail.xjtu.edu.cn (Y. Li), cfdkim@korea.ac.kr (J. Kim).
URL: http://gr.xjtu.edu.cn/web/yibaoli (Y. Li), http://math.korea.ac.kr/~cfdkim (J. Kim)

http://dx.doi.org/10.1016/j.mbs.2015.11.005
0025-5564/

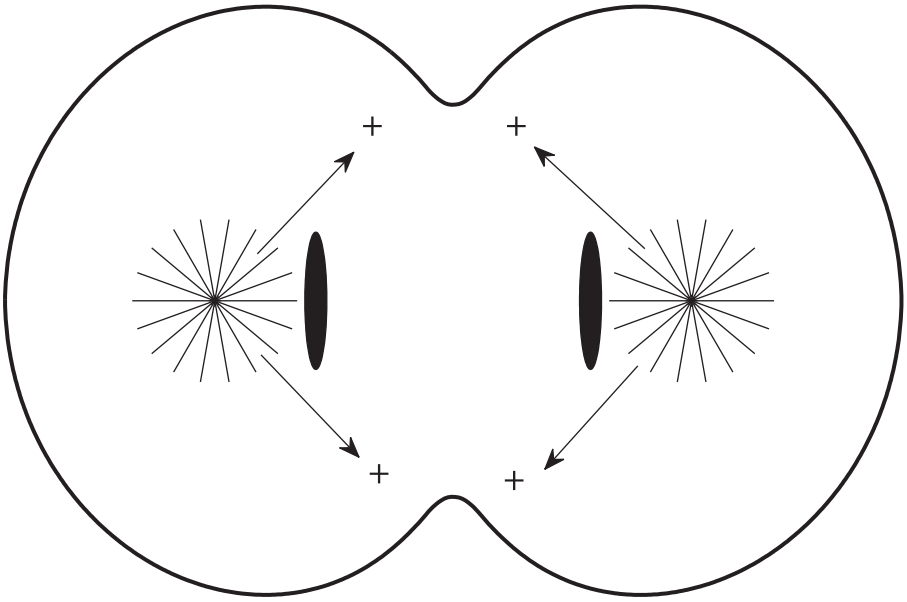

Fig. 1. Astral stimulation model. Since the equatorial cortex is influenced by astral microtubules from two poles, the strength of the stimulus should be maximal at the cell equator [1].

The remainder of this paper is organized as follows. In Section 2, we state the governing equations for animal cell growth and division. In Section 3, a fully discrete numerical method is given. In Section 4, we present numerical results such as the convergence of the scheme and effects of the model parameters. Finally, conclusions are drawn in Section 5.

2. Mathematical formulation

Let $\mathbf{X}(t)$ denote the immersed boundary point that describes the cell boundary, and let $\mathbf{Y}_1(t)$ and $\mathbf{Y}_2(t)$ represent the cell nuclei at time t. If the cell grows, two fluid sources $S_1(t)$ and $S_2(t)$ are located at the two cell nuclei. Once the cell doubles its volume, the sources are deactivated and the cell decides its division site to make the cleavage furrow. In animal cells, the structure that accomplishes cytokinesis is the contractile ring, which assembles just beneath the plasma membrane and contracts to constrict the cell into two. At the same time, a new membrane is inserted into the plasma membrane adjacent to the contractile ring by the fusion of intracellular vesicles. This membrane addition is necessary to compensate for the increased surface area that accompanies cytoplasmic division [29]. Therefore, for simplicity, we model the cell surface by the fluid interface. The complete system of equations describing cell growth and division in a viscous incompressible fluid is given by

$$\rho\left(\frac{\partial \mathbf{u}(\mathbf{x},t)}{\partial t}+\mathbf{u}(\mathbf{x},t)\cdot\nabla\mathbf{u}(\mathbf{x},t)\right)=-\nabla p(\mathbf{x},t)+\mu\Delta\mathbf{u}(\mathbf{x},t)+\frac{\mu\varsigma}{3\rho}\nabla S(\mathbf{x},t)+\sigma_1\mathbf{SF}(\mathbf{x},t)+\sigma_2\mathbf{DF}(\mathbf{x},t), \tag{1}$$

$$\rho\nabla\cdot\mathbf{u}(\mathbf{x},t)=\varsigma S(\mathbf{x},t), \tag{2}$$

where

$$S(\mathbf{x},t)=\sum_{m=1}^{2}(1-H(t-t_0))\delta_c(\mathbf{x}-\mathbf{Y}_m(t)), \tag{3}$$

$$\mathbf{SF}(\mathbf{x},t)=\int_\Gamma \mathbf{f}_1(\mathbf{X})\delta_c(\mathbf{x}-\mathbf{X}(\mathcal{A},t))d\mathcal{A}, \tag{4}$$

$$\mathbf{f}_1(\mathbf{X})=\kappa(\mathbf{X})\mathbf{n}(\mathbf{X}), \tag{5}$$

$$\mathbf{DF}(\mathbf{x},t)=\int_\Gamma \mathbf{f}_2(\mathbf{X}(\mathcal{A},t_0))\delta_c(\mathbf{x}-\mathbf{X}(\mathcal{A},t))d\mathcal{A}, \tag{6}$$

$$\mathbf{f}_2(\mathbf{X}(\mathcal{A},t_0))=\frac{H(t-t_0)\mathbf{n}_{div}(\mathbf{X}(\mathcal{A},t))}{s(\mathbf{X}(\mathcal{A},t_0))}, \tag{7}$$

$$s(\mathbf{X}(\mathcal{A},t_0))=\frac{\big||\mathbf{X}(\mathcal{A},t_0)-\mathbf{Y}_1(t_0)|-|\mathbf{X}(\mathcal{A},t_0)-\mathbf{Y}_2(t_0)|\big|}{\epsilon|\mathbf{Y}_1(t_0)-\mathbf{Y}_2(t_0)|}+1, \tag{8}$$

$$\mathbf{n}_{div}(\mathbf{X}(\mathcal{A},t))=\frac{(\mathbf{Y}_1(t_0)-\mathbf{X}(\mathcal{A},t))+(\mathbf{Y}_2(t_0)-\mathbf{X}(\mathcal{A},t))}{|(\mathbf{Y}_1(t_0)-\mathbf{X}(\mathcal{A},t))+(\mathbf{Y}_2(t_0)-\mathbf{X}(\mathcal{A},t))|}. \tag{9}$$

Lagrangian marker points move according to the following:

$$\frac{\partial\mathbf{X}}{\partial t}=\mathbf{U}(\mathbf{X}), \tag{10}$$

$$\mathbf{U}(\mathbf{X})=\int_\Omega \mathbf{u}(\mathbf{x})\delta_c(\mathbf{x}-\mathbf{X})d\mathbf{x}, \tag{11}$$

$$\frac{\partial\mathbf{Y}_m}{\partial t}=\mathbf{U}(\mathbf{Y}_m),\ \text{for } m=1,2, \tag{12}$$

$$\mathbf{U}(\mathbf{Y}_m)=\int_\Omega \mathbf{u}(\mathbf{x},t)\delta_c\mathbf{x}-\mathbf{Y}_m(t))d\mathbf{x}. \tag{13}$$

Here, $\mathbf{x}=(x,y,z)$ is the fixed Cartesian coordinate, and $\mathbf{X}$ is the Lagrangian variable for the immersed boundary (see Fig. 2). Eqs. (1) and (2) are the Navier–Stokes equations, which are the basic governing equations of a viscous incompressible Newtonian fluid [25,30]. In Eqs. (1) and (2), the physical parameters ρ and μ correspond to the constant mass density and constant viscous coefficient of the fluid, respectively, σ_1 and σ_2 correspond to the stiffness coefficient for the curvature force and division force, respectively. Moreover, p is the pressure, and $\mathbf{u}=(u,v,w)$ is the fluid velocity.

In Eq. (3), $S(\mathbf{x},t)$ represents the time-dependent source. $S(\mathbf{x},t)$ is positive around cell nuclei and zero on the other fluid domain when the cell grows. The sources are deactivated when the cell volume is doubled [13]. To model these states, we use the Heaviside function $H(t)$, where $H(t)=1$ when $t\geq 0$, and $H(t)=0$, otherwise. $\delta_c(\mathbf{x})$ is the three-dimensional smoothed Dirac delta function [26,31], which

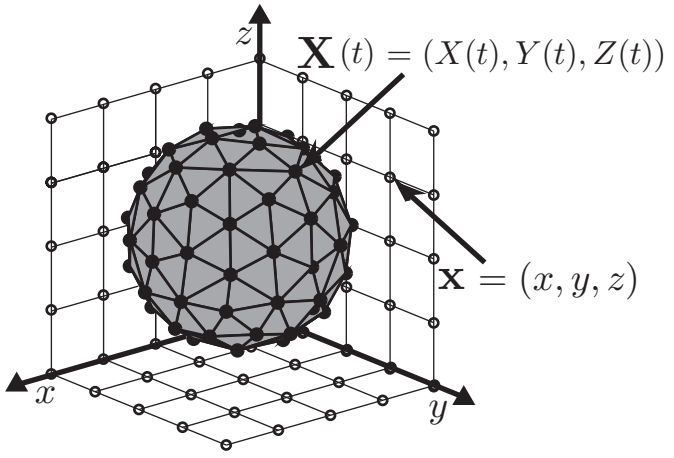

Fig. 2. Illustration of Eulerian points **x** and Lagrangian points **X**(t).

is defined by the product of one-dimensional smoothed Dirac delta functions, i.e.,

$$\delta_c(\mathbf{x}) = \frac{1}{c^3}\psi\left(\frac{x}{c}\right)\psi\left(\frac{y}{c}\right)\psi\left(\frac{z}{c}\right), \tag{14}$$

where c is the mesh width, h, and

$$\psi(r) = \begin{cases} (3 - 2|r| + \sqrt{1 + 4|r| - 4r^2})/8 & \text{if } |r| \le 1, \\ (5 - 2|r| - \sqrt{-7 + 12|r| - 4r^2})/8 & \text{if } 1 < |r| \le 2, \\ 0 & \text{if } |r| > 2. \end{cases} \tag{15}$$

Here, t_0 denotes the specific time when the mass of the cell doubles the size of its mother cell. Furthermore, ς is a positive value, $\mathbf{SF} = (SF_1, SF_2, SF_3)$ is the interfacial tension body force concentrated on the interface, $\mathbf{f}_1(\mathbf{X})$ is the interfacial force density, $\boldsymbol{\kappa}(\mathbf{X})$ is the mean curvature, $\mathbf{n}$ is the unit outward normal vector, and $\mathbf{DF}(\mathbf{x}, t)$ is the external force. The external force density $\mathbf{f}_2(\mathbf{X})$ in Eq. (7) is zero when $t < t_0$ to simulate the process of cell growth. When $t \ge t_0$, $\mathbf{f}_2(\mathbf{X})$ is $\mathbf{n}_{\text{div}}/s$. $s(\mathbf{X})$ is the proposed stimulus in the previous paper [24], which is defined as the difference of distances from two aster centers to the cell membrane and a control parameter ϵ. To ensure that the minimum of the stimulus function $s(\mathbf{X}(\mathcal{A}, t_0))$ is one, we set $s(\mathbf{X}(\mathcal{A}, t_0)) = \big||\mathbf{X}(\mathcal{A}, t_0) - \mathbf{Y}_1(t_0)| - |\mathbf{X}(\mathcal{A}, t_0) - \mathbf{Y}_2(t_0)|\big| / (\epsilon|\mathbf{Y}_1(t_0) - \mathbf{Y}_2(t_0)|) + 1$. In this case, $s(\mathbf{X})$ is in $[1, 1 + 1/\epsilon]$ and the maximum and minimum divisional forces are 1 at the cell equator and $1/(1 + 1/\epsilon)$ at the cell poles, respectively. We briefly discuss this phenomenon since a similar proof was proposed in [24]. Fig. 3 shows the schematic illustration of the external force. Fig. 3(a) shows the distribution of the proposed stimulus model $s(\mathbf{x})$, which is computed using the difference of distances from aster centers to the cell membrane and a control parameter ϵ. Fig. 3(b) shows the quiver of $\mathbf{n}_{\text{div}}(\mathbf{X})$, which is related to the positions of aster centers, and Fig. 3(c) shows our proposed external force $\mathbf{n}_{\text{div}}(\mathbf{X})/s(\mathbf{X})$. Note that in our proposed method, we assume that the resistive force from the membrane other than that of the contractile ring is surface tension, which means that these cells behave like water droplets, and the lipid bilayers of the cell membrane are allowed to stretch. If the lipid bilayers are inextensible, another external force that forces the cell to its original cell or maintains the surface area conservation should be added. A different value of ϵ can be chosen to change the length of the cell bridge as shown in Fig. 4. Note that as $\epsilon \to 0$, our model is the same as Rejniak's model [13], in which the author proposed a singular contractile ring located orthogonally to the axis of two cell nuclei.

In order to make the variables dimensionless, we define

$$x' = \frac{x}{L_c}, \quad \mathbf{u}' = \frac{\mathbf{u}}{U_c}, \quad t' = \frac{tU_c}{L_c}, \quad p' = \frac{p}{\rho_c U_c{}^2},$$

$$\rho' = \frac{\rho}{\rho_c}, \quad \varsigma' = \frac{U_c\varsigma}{\rho_c L_c},$$

where L_c, U_c, and ρ_c, are the characteristic length, velocity, and density, respectively. Substituting these variables into the governing Eqs. (1) and (2), and then omitting the primes yields

$$\mathbf{u}_t + \mathbf{u}\cdot\nabla\mathbf{u} = -\nabla p + \frac{1}{Re}\Delta\mathbf{u} + \frac{1}{Se}\nabla S + \frac{1}{We}\mathbf{SF} + \frac{1}{De}\mathbf{DF}, \tag{16}$$

$$\nabla\cdot\mathbf{u} = \varsigma S. \tag{17}$$

The dimensionless parameters are the Reynolds number, *Re*, Weber number, *We*, new parameter numbers, *De* and *Se*, which are given by

$$Re = \frac{\rho_c U_c L_c}{\mu}, \quad We = \frac{\rho_c U_c^2 L_c}{\sigma_1}, \quad De = \frac{\rho_c U_c^2 L_c}{\sigma_2}, \quad Se = \frac{3\rho_c U_c^2}{\mu L_c \varsigma}.$$

3. Numerical method

To compute the fluid flow interacting with an immersed boundary, two distinct discretized grids are needed that are regular lattice points for the whole fluid domain and boundary points for the

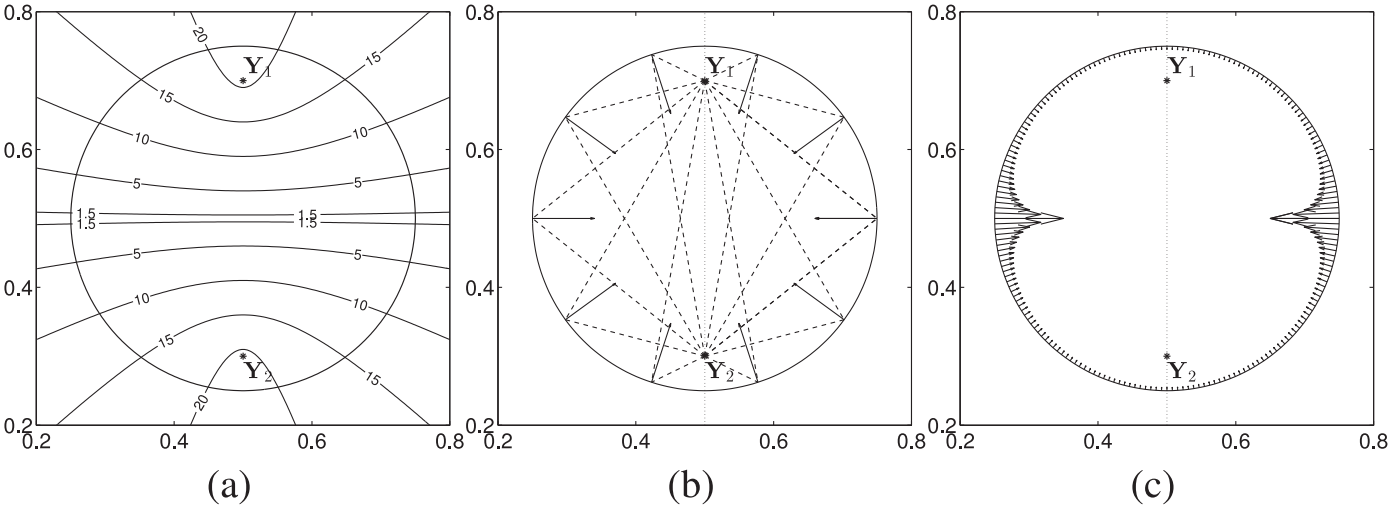

Fig. 3. Schematic for the external force from the cell membrane. (a) The proposed stimulus model $s(\mathbf{x})$ when $\epsilon = 0.05$, (b) the quiver of $\mathbf{n}_{\text{div}}(\mathbf{X})$, and (c) the proposed external force $\mathbf{n}_{\text{div}}(\mathbf{X})/s(\mathbf{X})$.

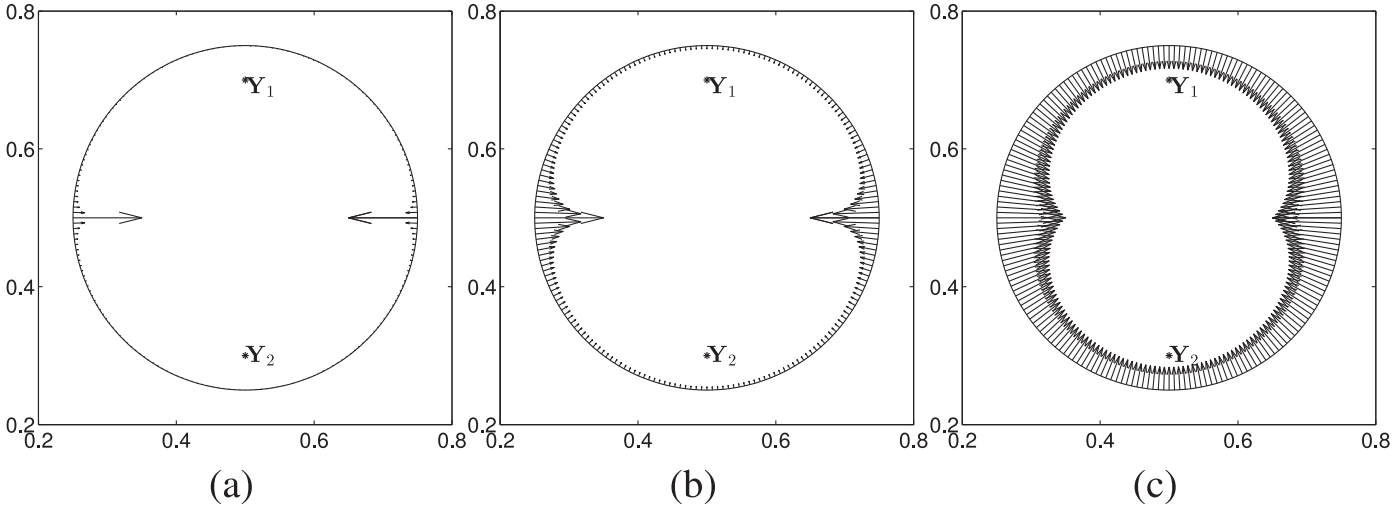

Fig. 4. Schematic for the external force from the cell membrane with various ϵ values. (a) $\epsilon = 0.005$, (b) $\epsilon = 0.05$, and (c) $\epsilon = 0.5$.

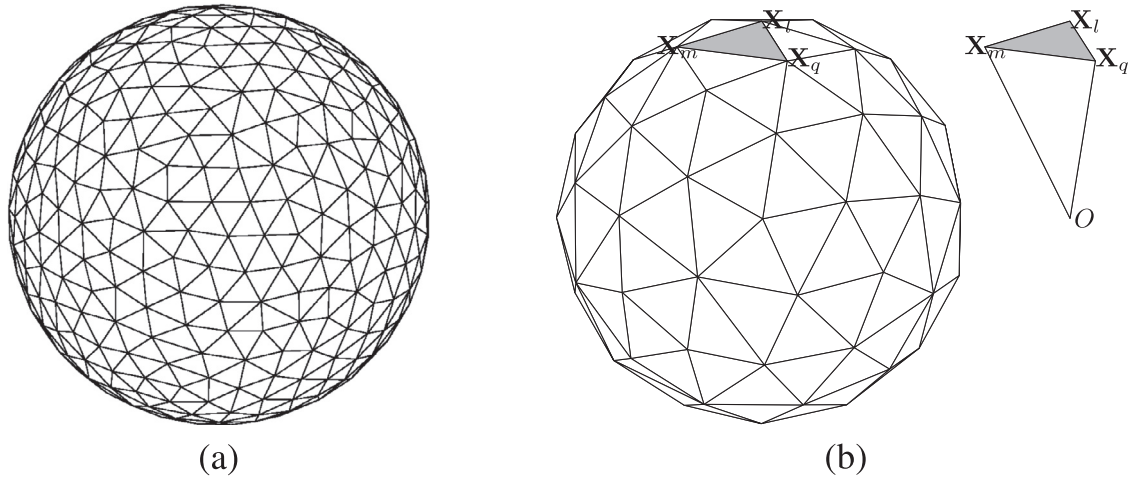

Fig. 5. (a) Triangular surface mesh obtained using the distmesh algorithm. (b) Schematic illustration of a polyhedron and tetrahedron with reference point **O**.

immersed boundary. First, consider the fluid domain $\Omega = [0, L_x] \times [0, L_y] \times [0, L_y]$ and define the fluid variables on a fixed $N_x \times N_y \times N_z$ Eulerian grid that is labeled as $\mathbf{x}_{ijk} = (x_i, y_j, z_k) = ((i-0.5)h, (j-0.5)h, (k-0.5)h)$ for $i = 1, \ldots, N_x$, $j = 1, \ldots, N_y$, and $k = 1, \ldots, N_z$, where h is the uniform mesh spacing, and N_x, N_y and N_z are the numbers of cells in the x, y, and z-directions, respectively. Denote the final time by T and the time step by Δt.

We solve the governing equations by the finite difference method on a staggered marker-and-cell mesh. The pressure and indicator functions are located at the cell centers, while the velocity components u, v, and w are placed at the centers of the x-, y-, and z-directional cell faces at the face centers, respectively; that is, $u_{i+\frac{1}{2},jk} = u(x_{i+\frac{1}{2}}, y_j, z_k)$, $v_{i,j+\frac{1}{2},k} = (x_i, y_{j+\frac{1}{2}}, z_k)$, and $w_{ij,k+\frac{1}{2}} = (x_i, y_j, z_{k+\frac{1}{2}})$. We assume a homogeneous Neumann boundary condition for the velocity. Moreover, we consider a set of M Lagrangian points $\mathbf{X}_l = (X_l, Y_l, Z_l)$ for $l = 1, \ldots, M$ that represents the immersed boundary. Suppose that there are M_T triangles $\mathbf{Tri}_s = (\mathbf{X}_l, \mathbf{X}_m, \mathbf{X}_q)$ for $s = 1, \ldots, M_T$. To generate an oriented triangular mesh connecting with immersed boundary points, we use the distmesh algorithm [32,33]. For more details, refer to [28,32,33]. The triangular surface mesh obtained using the distmesh algorithm is shown in Fig. 5(a). Notice that the immersed boundary is discretized using a set of uniform triangular grids and that the three vertices $\mathbf{X}_l$, $\mathbf{X}_m$, and $\mathbf{X}_q$ are ordered counterclockwise (see Fig. 5(b)).

Note that the reference time t_0 is defined as $m\Delta t$. Here, m is the integer that satisfies $V(\mathbf{X}^m) \geq 2V(\mathbf{X}^0)$ and $V(\mathbf{X}^{m-1}) < 2V(\mathbf{X}^0)$. $V(\mathbf{X})$ is the volume of the polyhedron. For all of the triangles on the surface $\mathbf{Tri}_s = (\mathbf{X}_l, \mathbf{X}_m, \mathbf{X}_q) = ((X_l, Y_l, Z_l), (X_m, Y_m, Z_m), (X_q, Y_q, Z_q))$ with a reference point (**O**) (see Fig. 5(b)), the volume of the polyhedron is given by

$$V(\mathbf{X}) = \frac{1}{6}\sum_{s=1}^{M_T}\Big[X_q(Y_lZ_m - Y_mZ_l) - Y_q(X_lZ_m - X_mZ_l) + Z_q(X_lY_m - X_mY_l)\Big].$$

Our goal is to compute $\mathbf{u}^{n+1}$, $\mathbf{X}^{n+1}$, and $\mathbf{Y}^{n+1}$ from given $\mathbf{u}^n$, $\mathbf{X}^n$, and $\mathbf{Y}^n$. This is done as follows:

Step 1. Using the positions of the cell boundary $\mathbf{X}^n$, and the two astral centers $\mathbf{Y}_1^n$ and $\mathbf{Y}_2^n$, we calculate two forces $\mathbf{SF}^n$ and $\mathbf{DF}^n$ using discretizations of Eqs. (5), (7), and (9). Note that the normal mean curvature, $\kappa_l^n \mathbf{n}_l^n$, is calculated using the algorithm in [28,34,35].

Step 2. Spread the force into the nearby grid points of the fluid by using a discretization of Eqs. (4) and (6):

$$\mathbf{SF}_{ijk}^n = \sum_{l=1}^{M} \mathbf{f}_{1l}^n \delta_h(\mathbf{x}_{ijk} - \mathbf{X}_l^n)\Delta\mathcal{A}_l,$$

$$\mathbf{DF}_{ijk}^n = \sum_{l=1}^{M} \mathbf{f}_{2l}^n \delta_h(\mathbf{x}_{ijk} - \mathbf{X}_l^n)\Delta\mathcal{A}_l,$$

$$\text{for } i = 1, \ldots, N_x,\ j = 1, \ldots, N_y,\ k = 1, \ldots, N_z.$$

Step 3. Solve the Navier–Stokes equations (16) and (17) using a projection method. First, we solve for an intermediate velocity field $\tilde{\mathbf{u}}$ without the pressure gradient term;

$$\frac{\tilde{\mathbf{u}}-\mathbf{u}^n}{\Delta t}+\mathbf{u}^n\cdot\nabla_d\mathbf{u}^n=\frac{1}{Re}\Delta_d\mathbf{u}^n+\frac{1}{We}\mathbf{SF}^n+\frac{1}{De}\mathbf{DF}^n+\frac{1}{Se}\nabla_d S^n.$$

Then, we solve the following equations for the advanced pressure field at the $(n+1)$st time step:

$$\frac{\mathbf{u}^{n+1}-\tilde{\mathbf{u}}}{\Delta t}=-\nabla_d p^{n+1}, \tag{18}$$

$$\nabla_d\cdot\mathbf{u}^{n+1}=\varsigma S^n. \tag{19}$$

By applying the divergence operator to Eq. (18), we are able to determine the Poisson equation for the pressure at the advanced time $(n+1)$:

$$\Delta_d p^{n+1}=\frac{1}{\Delta t}(\nabla_d\cdot\tilde{\mathbf{u}}-\varsigma S^n). \tag{20}$$

The resulting linear system of Eq. (20) is solved using a multigrid method; specifically, V-cycles with Gauss–Seidel relaxation. Then, the divergence-free normal velocities u^{n+1}, v^{n+1}, and w^{n+1} are defined by

$$\mathbf{u}^{n+1}=\tilde{\mathbf{u}}-\Delta t\nabla_d p^{n+1}.$$

Step 4. Once the updated fluid velocity $\mathbf{u}^{n+1}$ has been determined, the velocity on the immersed boundary $\mathbf{U}^{n+1}$, immersed boundary points $\mathbf{X}^{n+1}$, and center positions $\mathbf{Y}^{n+1}$ are determined. These are calculated using the discretizations of Eqs. (10)–(13).

These steps complete the description of the process by which the quantities **u, X**, and **Y** are updated.

3.1. Volume correction algorithm

Cytokinesis is usually the shortest part of the cell cycle. It is during interphase (G_1, S, and G_2 phases) that the cell grows by producing proteins and cytoplasmic organelles such as mitochondria and endoplasmic reticulum [36]. Therefore, during cytokinesis, the mass of the cell changes very little. Thus, in order to conserve the mass of the cell during the cytokinesis, we use a volume-preserving scheme [28]. Note that there are other volume-conserving methods [37–39] in conjunction with immersed boundary equations. The key idea of the method is relocating surface points along the normal directions to conserve the total volume. A brief description of the volume correction procedure is summarized below.

Step (1). Update the immersed boundary points $\mathbf{X}^*$ according to Eq. (11); that is, $\mathbf{X}^*=\mathbf{X}^n+\Delta t\mathbf{U}^{n+1}$.

Step (2). Check the relative error of the volume $V(\mathbf{X}^*)$ defined by $V_{\text{error}}(\mathbf{X})=|2V(\mathbf{X}^0)-V(\mathbf{X})|/(2V(\mathbf{X}^0))$. For a given tolerance, tol, check whether $V_{\text{error}}(\mathbf{X}^*)<\text{tol}$ or not. If so, then $\mathbf{X}^{n+1}=\mathbf{X}^*$; otherwise, relocate the surface points along the normal directions, i.e., $\mathbf{X}^{n+1}=\mathbf{X}^*+\beta\mathbf{n}$, where β is a constant.

Step (3). Determine the parameter β, which is a root of the cubic equation $V(\mathbf{X}^{n+1})=V(\mathbf{X}^*+\beta\mathbf{n})=2V(\mathbf{X}^0)$ and update $\mathbf{X}^{n+1}=\mathbf{X}^*+\beta\mathbf{n}$. For more details, please refer to [28].

3.2. Remeshing algorithm for the surface mesh

During the numerical simulations, some interfaces are stretched or compressed. To preserve the high-quality surface mesh, we use the remeshing algorithm in [27]. A brief description of the remeshing algorithm is summarized below.

Step (1). Construct the signed distance function ϕ in the whole domain using the surface mesh $\mathbf{X}^n$ and set $\widetilde{\mathbf{X}}_l^{n,m}=\mathbf{X}_l^n$, where $m=0$.

Step (2). Calculate the net force $\mathbf{F}(\widetilde{\mathbf{X}}_l^{n,m})$ and update the intermediate position by $\mathbf{X}_l^*=\widetilde{\mathbf{X}}_l^{n,m}+\Delta\tau\mathbf{F}(\widetilde{\mathbf{X}}_l^{n,m})$, where $\Delta\tau$ is a constant. The net forces work in the following way: if the distance of two nearby points is smaller than a given value, the forces should be away from each other; otherwise, they should move toward each other.

Step (3). Project $\mathbf{X}_l^*$ to the interface, which is defined as the zero level of ϕ, and obtain the new point $\mathbf{X}_l^{n,m+1}$ on the interface by $\mathbf{X}_l^{n,m+1}=\mathbf{X}_l^*-\phi(\mathbf{X}_l^*)\nabla_d\phi(\mathbf{X}_l^*)$. The reaction forces $\phi(\mathbf{X}^*)\nabla_d\phi(\mathbf{X}^*)$ enter in the following way: all points that leave the interface during processing in *Step* (2) move back to the closest interface position along the normal vector $\nabla_d\phi(\mathbf{X}_l^*)$.

Step (2) and *Step* (3) are repeated until the discrete norm is smaller than a given tolerance value. We then complete the remeshing procedure for the surface mesh. Note that in our algorithm, remeshing is done at every 20 time-steps.

Fig. 6 (a) and (b) shows the triangular mesh before and after the remeshing procedure, respectively. From left to right, they are vertical and horizontal plane views. Before using the remeshing procedure, the mesh distribution in the pole and equatorial regions is not uniform. On the other hand, if the remeshing procedure is applied, then an almost uniform mesh is obtained. In Section 4, we will perform a numerical test to emphasize the effects of the remeshing algorithm on cell cytokinesis.

It is important to note that the shape of the cell surface should agree with the shape of the original object after the remeshing procedure. To verify this fact, we consider a numerical test with a sphere that is centered at (0.5, 0.5, 0.5) with a radius of 0.25 in a unit domain. The initial mesh distribution is not uniform as shown in Fig. 6(a). Here, $M=1024$ is used. The remeshing procedure is performed to obtain the new mesh. The theoretical value of the distance, which is computed from the point $\mathbf{X}$ on the surface to the center, is $|\mathbf{X}-(0.5,0.5,0.5)|=0.25$. We calculate the discrete l_2-norm of the error, which is $\sqrt{\sum_{l=1}^{M}(0.25-|\mathbf{X}_l-(0.5,0.5,0.5)|)^2/M}=4.71\text{e}-4$. These results indicate that the remeshing procedure preserves the shape of the cell surface.

Table 1
Computational parameters used in real biophysical experiments.

Parameter	Physical and biophysical quantity
Diameter of cell (D)	10–20 μm
Fluid density (ρ)	1.35 g/(cm^3) [13,21] [14,15]
Fluid viscosity (μ)	100 g/(cm s) [13–15], 50–140 g/(cm s) [18]
Surface tension (σ_1)	490–850 g/(cm s^2) [13], 0.42–1.4 $\times$ 10^4 g/(cm s^2) [22]
Contractile stress (σ_2)	0–10^6 g/(cm s^2) [21] 5 $\times$ 10^7 g/(cm s^2) [14]
Source strength (ς)	2 $\times$ 10^{-7}g/s [14]

4. Numerical experiments

Various papers have reported the real biophysical parameters in cell processes, which are summarized in Table 1. Note that the Reynolds number is much smaller than one. For different animal cells, the real parameters vary. In this paper, we use $Re=0.5$. To simplify the presentation, we use $We=1$ and $De=2\text{e}{-3}$, which are in the range of the real parameters. ϵ is the parameter that relates to the shape of the intercellular bridge [24]; here, we set $\epsilon=0.05$. A mesh grid of size $64\times64\times64$ is used on the computational domain $\Omega=(0,4)\times(0,4)\times(0,4)$. Unless otherwise specified, the initial shape of the cell is a unit sphere and 10,436 nodes represent the cell boundary. The time step chosen is $\Delta t=0.05h^2$. The astral centers are $Y_1=(2,1.8,2)$ and $Y_2=(2,2.2,2)$.

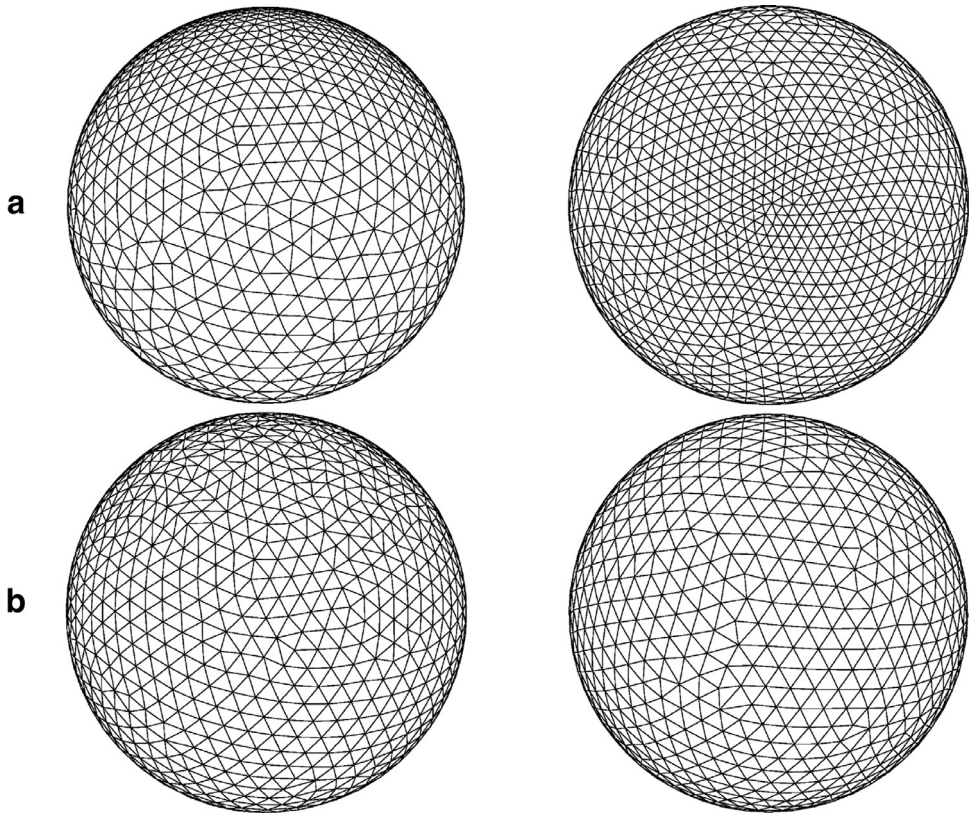

Fig. 6. Surface meshes (a) before and (b) after the remeshing procedure. From left to right, they are vertical and horizontal plane views.

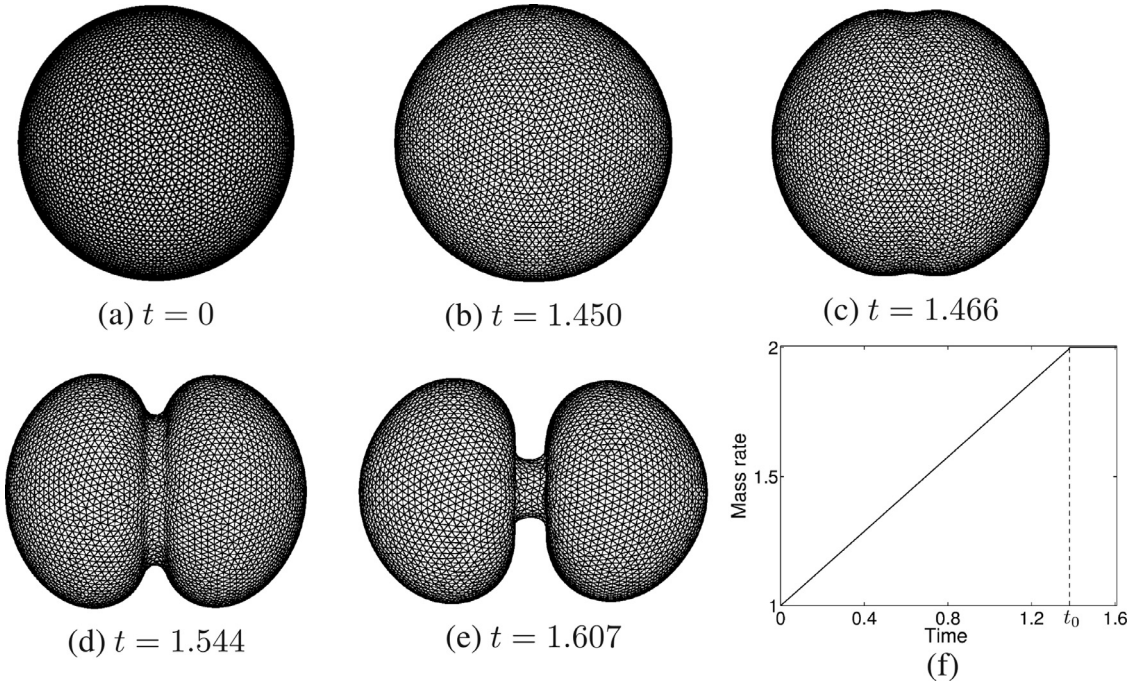

Fig. 7. (a)–(e) Evolution of cell growth and division. The computational times are listed below each figure. (f) Mass change rate, $V(\mathbf{X}^n)/V(\mathbf{X}^0)$.

4.1. Evolution of cell division

In this experiment, we show the evolution of cell division on the unit computational domain in three dimensions. The simulation is conducted up to time $T = 1.607$. The evolution is shown in Fig. 7(a)–(e), and the computational times are listed below each figure. Two point sources inside the cell make the cell grow (Fig. 7(a) and (b)). Once the cell volume doubles, the sources are deactivated, and the contracting force is activated. With the proposed division force, the cell is divided into two cells as shown in Fig. 7(c)–(e). When the sources are deactivated at time t_0, we assume that the mass of the cell is conservative. Exact mass

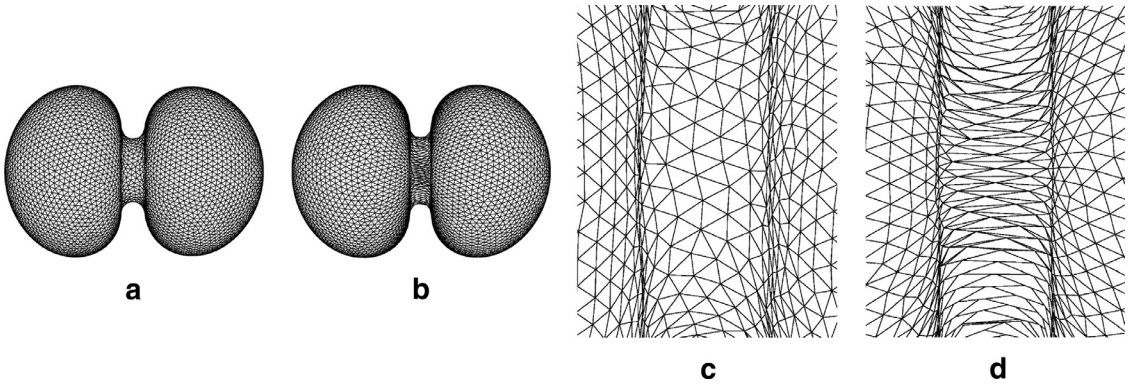

Fig. 8. Comparison of cell shapes at $T = 0.156$ with (a) and without (b) the remeshing process. (c) and (d) are the close-up views of (a) and (b), respectively.

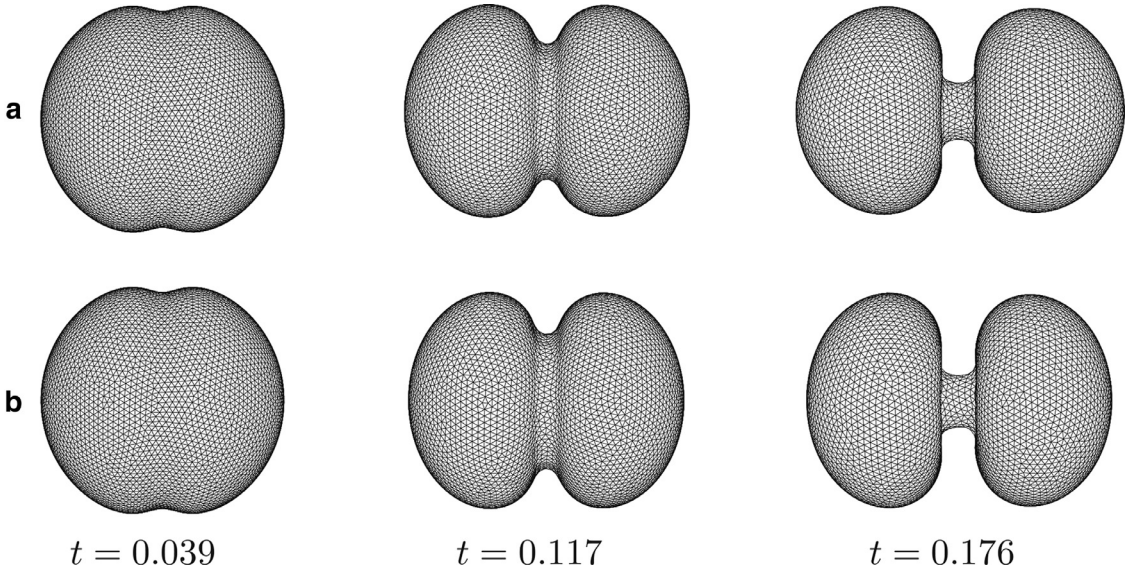

Fig. 9. Evolution of cell division with the advection term (a) and without the advection term (b) in Eq. (1).

conservation is achieved using the correction scheme, as shown in Fig. 7(f).

4.2. Effect of the remeshing procedure

Fig. 8 (a) and (b) shows the cell shapes at time $T = 0.156$ with and without the remeshing procedure, respectively. Parts (c) and (d) of Fig. 8 are the close-up views of (a) and (b), respectively. Here, we only consider the cell division step. Thus, the initial shape of the cell is a sphere with a diameter of 1.26. From the results shown in Fig. 8, note the excellent mesh quality throughout the evolution of the remeshing procedure in contrast to the elongated elements that can be seen when the remeshing procedure is not applied. The CPU times are 23.79 min and 19.36 min for the two cases, respectively. Thus, the fraction of time spent performing the remeshing procedure is not much higher compared to the whole computational process.

4.3. Convergence test

To calculate the convergence rate, we consider the same test problem set in Section 4.2. Here, the remeshing procedure is not considered. The numerical solutions are computed on uniform grids, where $h = 4/2^n$, for $n = 5$, 6, 7, and 8. We run the computational simulation up to time $T = 0.0025$ with corresponding time steps, $\Delta t = 0.01h^2$. We define the discrete l_2-norm error $e_{h/\frac{h}{2}}$ by $e_{h/\frac{h}{2}} = \sqrt{\frac{1}{M}\sum_{l=1}^{M} |\mathbf{X}_{h,l} - \mathbf{X}_{h/2,l}|^2}$. Here, $\mathbf{X}_{h/2,\,l}$ is the point $\mathbf{X}_{h,\,l}$ in the successively finer grid. The rate of convergence is defined as the ratio of successive errors, i.e., $\log_2(e_{h/\frac{h}{2}}/e_{\frac{h}{2}/\frac{h}{4}})$. Using these definitions, the errors and rates of convergence are calculated, as shown in Table 2. Note that our discretization is second-order in space and first order in time. By refining the spatial and temporal grids by a factor of four and two, respectively, the ratio of successive errors increases by a factor of two. Notice that the convergence rate is approximately second-order in space, which is expected from discretization. However, since the division force is defined based on the positions of the immersed points of the cell boundary and cell nuclei, nonlinear effects are added when the cell nuclei and immersed points move. The convergence rate slightly decreases, as shown in Table 2.

Table 2
Error and convergence rates with the remeshing procedure.

Grid size	32^3–64^3	64^3–128^3	128^3–256^3
$e_{h/\frac{h}{2}}$	7.009e−6	2.050e−6	5.647e−7
Rate	1.77	1.86	

4.4. Inertial effects in our proposed method

The vast majority of biological processes at the microscopic scale (including cell division) occur in the creeping flow regime. To investigate the inertial effects in our proposed method, we compare the

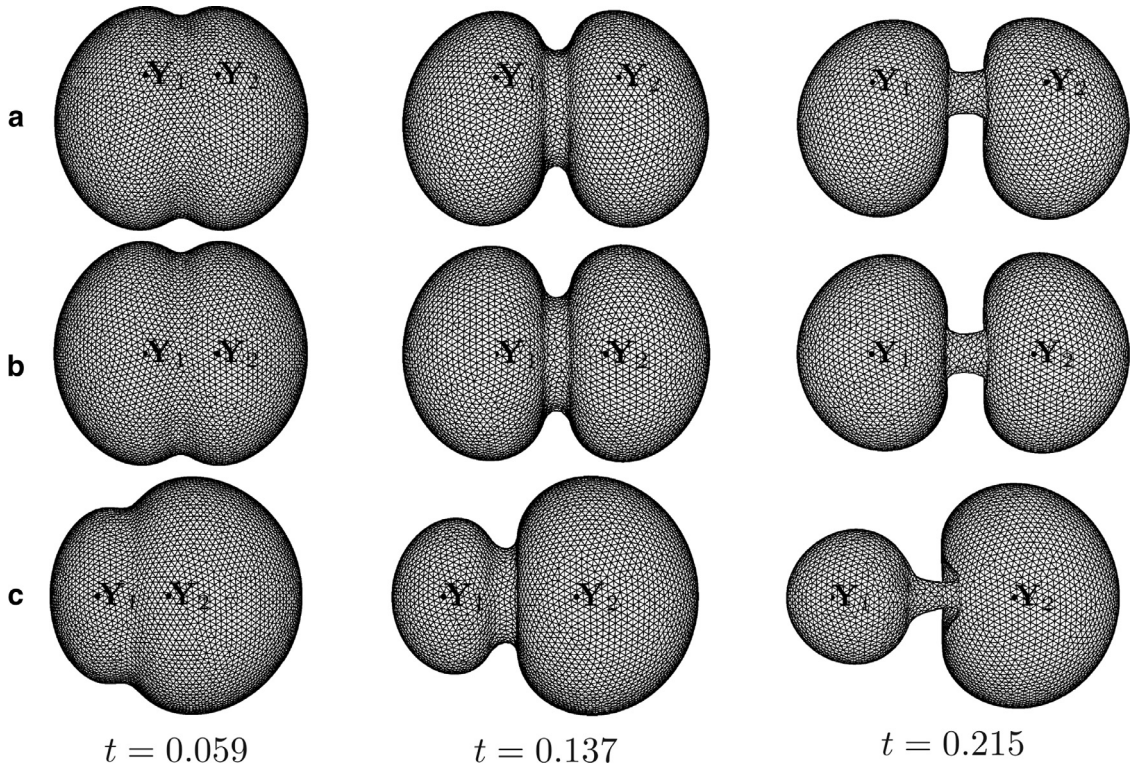

Fig. 10. Evolution of cell division with different aster positions. (a) $Y_1 = (2, 1.8, 2.4)$ and $Y_2 = (2, 2.2, 2.4)$, (b) $Y_1 = (2, 1.8, 2)$ and $Y_2 = (2, 2.2, 2)$, (c) $Y_1 = (2, 1.4, 2)$ and $Y_2 = (2, 1.8, 2)$.

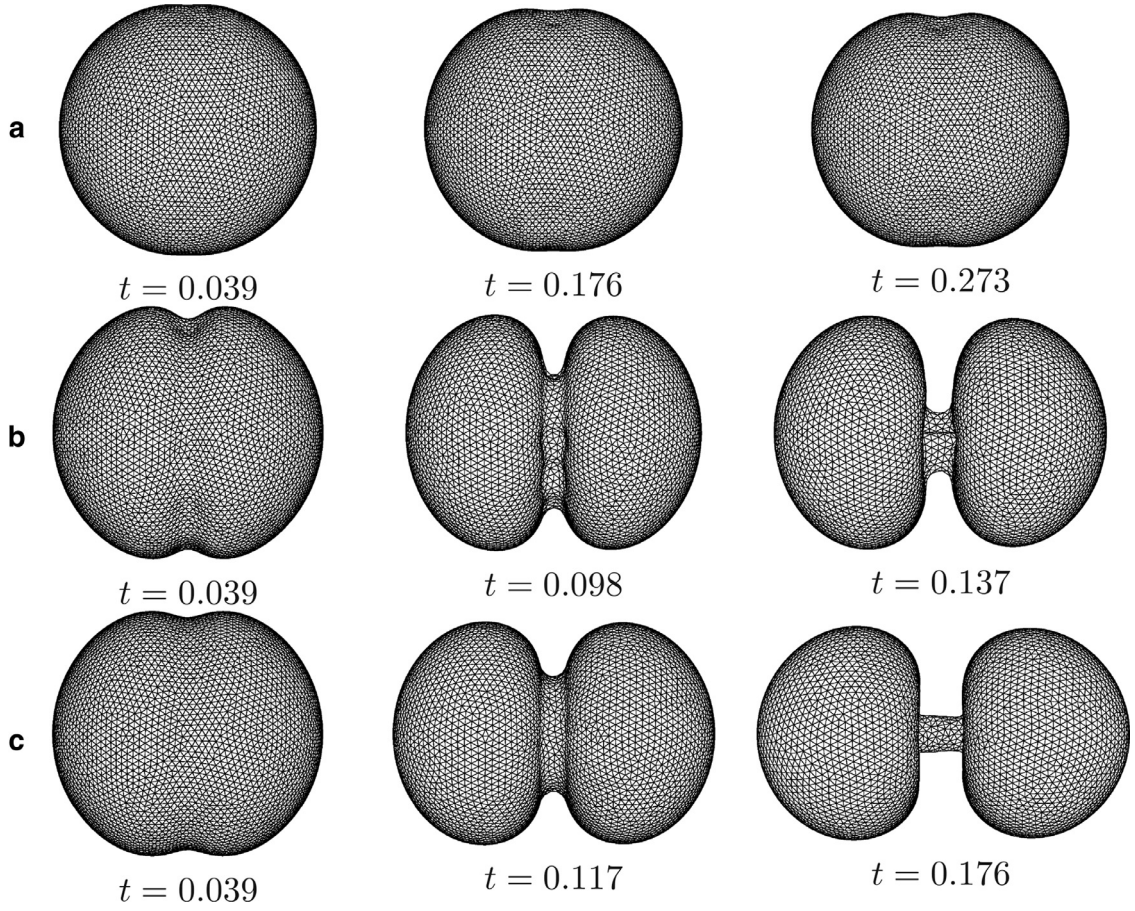

Fig. 11. Effect of ϵ. The computational times are shown below each figure. (a) $\epsilon = 0.005$ and $De = 2e{-}3$, (b) $\epsilon = 0.005$ and $De = 4e{-}4$, (c) $\epsilon = 0.1$ and $De = 2e{-}3$.

results obtained with and without the advection term in Eq. (1). Each calculation is conducted up to time $T = 0.176$. The other parameters and initial conditions are the same as those used in Section 4.2. Fig. 9 shows the evolutions of cell division with the advection term (a) and without the advection term (b). The results fit a straight line. The similar results obtained by the two cases imply that the inertial effects are negligible during cell division.

4.5. Symmetric and nonsymmetric cell divisions

For most animal cells, cell division is symmetric during cytokinesis and results in two equal daughter cells. During asymmetric division, an axis of polarity is established and the mitotic spindle reorients along the axis [5]. Several conserved proteins have been identified that are required for asymmetric divisions. However, a report [23] that analyzed the role of centrosomes and astral microtubules in Drosophila neuroblast divisions concluded that astral microtubules are not required for signaling or positioning cytokinesis, which is consistent with the spindle midzone being required for positioning the cleavage furrow [5,23]. Here, we consider symmetric and nonsymmetric cell divisions by choosing the astral centers to be $Y_1 = (2, 1.8, 2.4)$ and $Y_2 = (2, 2.2, 2.4)$, $Y_1 = (2, 1.8, 2)$ and $Y_2 = (2, 2.2, 2)$, and $Y_1 = (2, 1.4, 2)$ and $Y_2 = (2, 1.8, 2)$. The first two cases are for the symmetric cell divisions and the last one is for nonsymmetric case. The evolution of the three cases is shown in Fig. 10. These results suggest that our proposed mathematical model performs well in simulating cell division and agrees well with [23], where asterless neuroblasts assemble cytokinetic rings around the central spindle midzone and undergo unequal cytokinesis.

4.6. Simulation of the cell bridge

In the last stage of animal cell division called cytokinesis, the intercellular bridge between the two daughter cells thins and severs, and the mechanical separation of a mother cell in two daughter cells occurs [40]. In general, the intercellular bridge is formed in the middle of the cell due to the cleavage furrow constricting; thus, a good mathematical model should properly define the cleavage furrow, which can lead to the formation of a cylindrical bridge. To investigate the formation of the intercellular bridge in the cell division by process, we simulate cell division using two values of $\epsilon = 0.005$ and 0.1. Fig. 11(a) and (b) shows the evolution of cell division for $De = 2e{-}3$ and $De = 4e{-}4$, respectively. Here $\epsilon = 0.005$ is used. Notice that when ϵ is smaller, the contractile stress, De, increases to make the mother cell split into two separate daughter cells. Furthermore, the division time decreases as De decreases. Compared with the results in Fig. 11(c), which are obtained using $\epsilon = 0.1$ and $De = 2e{-}3$, a larger ϵ value makes the intercellular bridge longer.

5. Conclusion

We proposed an immersed boundary method to simulate eukaryotic cell growth and cytokinesis in three dimensions. Triangular meshes were employed to represent the cell membrane, and nodes were used for the Lagrangian points to track the motion. To prevent the mesh from being distorted, a surface remeshing algorithm was applied, which allowed for sufficient evolution for cytokinesis. To maintain the mass of the cell in cytokinesis, we used a volume-conserving algorithm. Various numerical experiments were performed to demonstrate the ability of the proposed method to model the cell growth and division process. In our proposed method, we assumed that the resistive force from the membrane other than that of the contractile ring was surface tension, which means that these cells behave like water droplets, and the lipid bilayers of the cell membrane are allowed to stretch; however, the lipid bilayers can also be inextensible for cells such as red blood cells. In this framework, another external force, which forces the cell to its original cell or conserves the surface area, should be added. In [41], the authors developed an immersed boundary method to simulate the dynamics of the inextensible vesicles with the new elastic force, which is derived from the variational derivative of the proposed elastic energy to resist bending the membrane, tension energy to enforce the surface area constraint, and other energy functions for biology justifications. As future research, it would be interesting to consider a membrane that stretches and studies the effects of the external forces during cell cytokinesis. In this paper, we adopt the mathematical model suggested by Rejniak [13]. Effectively, two fluid sources push each other, resulting in two new nuclei are placed along the cells' longest axis. We also plan to consider biological modelling and simulation of cell growth. One part is that flows into the cell through the cell membrane and another part would be that producing proteins and cytoplasmic organelles such as mitochondria and endoplasmic reticulum.

Acknowledgments

Y.B. Li is supported by the Fundamental Research Funds for the Central Universities, China (no. XJJ2015068) and supported by China Postdoctoral Science Foundation, China (no. 2015M572541). The corresponding author (J.S. Kim) was supported by the National Research Foundation of Korea, South Korea (NRF) grant funded by the Korea government (MSIP) (NRF-2014R1A2A2A01003683). The authors would like to thank Jung-il Choi, Darae Jeong, Jaemin Shin, and Hakyu Song for their very helpful comments on this paper. The authors are also grateful for the reviewers whose valuable suggestions and comments have significantly improved the quality of this paper.

References

[1] M. Glotzer, Cleavage furrow positioning, J. Cell Biol. 164 (3) (2004) 347–351.
[2] N.A. Campbell, J.B. Reece, Biology, 7th, Benjamin Cummings, San Francisco, CA, 2005.
[3] L. Foucard, X. Espinet, E. Benet, F.J. Vernerey, The Role of the Cortical Membrane in Cell Mechanics: Model and Simulation, John Wiley & Sons Ltd, Oxford, 2013.
[4] D. Gonze, The role of the cortical membrane in cell mechanics: model and simulation, J. Theor. Biol. 325 (2013) 22–33.
[5] D.A. Guertin, S. Trautmann, D. McCollum, Cytokinesis in eukaryotes, Microbiol. Mol. Biol. Rev. 66 (2002) 155–178.
[6] M. Haltera, J.T. Elliotta, J.B. Hubbarda, A. Tonab, A.L. Planta, Cell volume distributions reveal cell growth rates and division times, J. Theor. Biol. 257 (2009) 124–130.
[7] Y. Kim, H.G. Othmer, A hybrid model of tumor–stromal interactions in breast cancer, Bull. Math. Biol. 75 (2013) 1304–1350.
[8] M. Phllippe, Existence of a solution to the cell division eigenproblem, Math. Models Methods Appl. Sci. 16 (2006) 1125–1153.
[9] G.M.A. Phillipsa, P.R. Shorten, G.C. Wake, J. Guan, Modeling the effect of insulin-like growth factor-1 on human cell growth, Math. Biosci. 259 (2015) 43–54.
[10] J.D. Murray, G.F. Oster, A.K. Harris, A mechanical model for mesenchymal morphogenesis, J. Math. Biol. 17 (1983) 125–129.
[11] R. Rappaport, Establishment of the mechanism of cytokinesis in animal cells, Int. Rev. Cytol. 105 (1986) 245–281.
[12] R. Rappaport, Cytokinesis in Animal Cells, Cambridge University Press, England, 1996.
[13] K.A. Rejniak, A single-cell approach in modeling the dynamics of tumor microregions, Math. Biosci. Eng. 2 (2012) 643–655.
[14] K.A. Rejniak, An immersed boundary framework for modelling the growth of individual cells: an application to the early tumour development, J. Theor. Biol. 247 (2007) 186–204.
[15] K.A. Rejniak, A.R.A. Anderson, A computational study of the development of epithelial acini: I. Sufficient conditions for the formation of a hollow structure, Bull. Math. Biol. 70 (2008) 677–712.
[16] J. Leedale, A. Herrmannb, J. Bagnallb, A. Fercherc, D. Papkovskyc, V. Seb, R.N. Bearon, Modeling the dynamics of hypoxia inducible factor-1 (HIF-1) within single cells and 3D cell culture systems, Math. Biosci. 258 (2014) 33–43.
[17] L.L. Satterwhite, T.D. Pollard, Cytokinesis, Curr. Opin. Cell Biol. 4 (1992) 43–52.
[18] V.M. Laurent, E. Planus, R. Fodil, D. Isabey, Mechanical assessment by magnetocytometry of the cytosolic and cortical cytoskeletal compartments in adherent epithelial cells, Biorheology 40 (2003) 235–240.
[19] J.J. Tyson, K.B. Hannsgen, Cell growth and division: a deterministic/probabilistic model of the cell cycle, J. Math. Biol. 23 (1986) 231–246.
[20] J.J. Devore, G.W. Conrad, R. Rappaport, A model for astral stimulation of cytokinesis in animal cells, J. Cell Biol. 109 (1989) 2225–2232.

[21] M. Dembo, F. Harlow, Cell motion, contractile networks, and the physics of interpenetrating reactive flow, Biophys. J. 50 (1986) 109–121.
[22] A. Park, D. Koch, R. Cardenas, J. Kas, C.K. Shi, Cell motility and local viscoelasticity of fibroblasts, Biophys. J. 89 (2005) 4330–4342.
[23] M.G. Giansanti, M. Gatti, S. Bonaccorsi, The role of centrosomes and astral microtubules during asymmetric division of Drosophila neuroblasts, Development 128 (2001) 1137–1145.
[24] Y.B. Li, A. Yun, J.S. Kim, An immersed boundary method for simulating a single axisymmetric cell growth and division, J. Math. Biol. 65 (2012) 653–675.
[25] C.S. Peskin, Numerical analysis of blood flow in the heart, J. Comput. Phys. 25 (1977) 220–252.
[26] M.C. Lai, C. Peskin, An immersed boundary method with formal second-order accuracy and reduced numerical viscosity, J. Comput. Phys. 160 (2000) 705–719.
[27] H. Hua, Y.B. Li, J. Shin, H. Song, J.S. Kim, Effect of confinement on droplet deformation in shear flow, Int. J. Comput. Fluid D. 27 (2013) 317–331.
[28] Y.B. Li, A. Yun, D. Lee, J. Shin, D. Jeong, J.S. Kim, Three-dimensional volume-conserving immersed boundary model for two-phase fluid flows, Comput. Methods Appl. Mech. Eng. 257 (2013) 36–46.
[29] B. Alberts, A. Johnson, J. Lewis, M. Raff, K. Roberts, P. Walter, Molecular Biology of the Cell, 4th, Garland Science, New York, 2002.
[30] G.K. Batchelor, An Introduction to Fluid Dynamics, Cambridge University Press, 2000.
[31] S. Lim, Dynamics of an open elastic rod with intrinsic curvature and twist in a viscous fluid, Phys. Fluids 22 (2010) 024104.
[32] P.O. Persson, G. Stangt, A simple mesh generator in MATLAB, SIAM Rev. Soc. Ind. Appl. Math. 46 (2004) 329–345.
[33] P.O. Persson, Mesh size functions for implicit geometries and PDE-based gradient limiting, Eng. Comput. 22 (2006) 95–109.
[34] M. Belkin, J. Sun, Y. Wang, Discrete laplace operator on meshed surfaces, in: Proceedings of 24th Annual ACM Symposium on Computational Geometry, 2003, pp. 278–287.
[35] M. Meyer, M. Desbrun, P. Schröder, A.H. Barr, Discrete differential-geometry operators for triangulated 2-manifolds, Math. Vis. 3 (2002) 52–58.
[36] N.A. Campbell, J.B. Reece, L.A. Urry, M.L. Cain, S.A. Wasserman, P.V. Minorsky, R.B. Jackson, Biology, 8th, Pearson/Benjamin Cummings, San Francisco, 2008.
[37] C.S. Peskin, B.F. Printz, Improved volume conservation in the computation of flows with immersed elastic boundaries, J. Comput. Phys. 105 (1) (1993) 33–46.
[38] B.E. Griffith, On the volume conservation of the immersed boundary method, Commun. Comput. Phys. 12 (2) (2012) 401–432.
[39] J.H. Seo, R. Mittal, A sharp-interface immersed boundary method with improved mass conservation and reduced spurious pressure oscillations, J. Comput. Phys. 230 (19) (2011) 7347–7363.
[40] A.V. Kuzetsov, P. Xiang, Numerical investigation of thinning of the intercellular bridge during cell cytokinesis, Int. J. Heat Mass Transf. 33 (2006) 1071–1078.
[41] W.-F. Hu, Y. Kim, M.-C. Lai, An immersed boundary method for simulating the dynamics of three-dimensional axisymmetric vesicles in Navier–Stokes flows, J. Comput. Phys. 257 (2014) 670–686.